

Observation of heat scaling across a first-order quantum phase transition in a spinor condensate

H.-Y. Liang,^{*} L.-Y. Qiu,^{*} Y.-B. Yang, H.-X. Yang, T. Tian, Y. Xu,[†] and L.-M. Duan[‡]
Center for Quantum Information, IIIS, Tsinghua University, Beijing 100084, PR China

Heat generated as a result of the breakdown of an adiabatic process is one of the central concepts of thermodynamics. In isolated systems, the heat can be defined as an energy increase due to transitions between distinct energy levels. Across a second-order quantum phase transition (QPT), the heat is predicted theoretically to exhibit a power-law scaling, but it is a significant challenge for an experimental observation. In addition, it remains elusive whether a power-law scaling of heat can exist for a first-order QPT. Here we experimentally observe a power-law scaling of heat in a spinor condensate when a system is linearly driven from a polar phase to an antiferromagnetic phase across a first-order QPT. We experimentally evaluate the heat generated during two non-equilibrium processes by probing the atom number on a hyperfine energy level. The experimentally measured scaling exponents agree well with our numerical simulation results. Our work therefore opens a new avenue to experimentally and theoretically exploring the properties of heat in non-equilibrium dynamics.

In quantum mechanics, at zero temperature, when we drive an isolated system by tuning a system parameter, if the driving rate is so slow such that the process is adiabatic, the transition between energy levels cannot occur, and heat cannot be created. Yet, when the system undergoes a second-order QPT during the process, the relaxation time diverges and thus adiabaticity cannot be maintained. As a result, transition between energy levels does occur, producing the heat [1, 2]. In fact, across the transition point, the physics can be described by the quantum Kibble-Zurek mechanism (KZM) and universal scaling laws for various quantities, such as the temporal onset of excitations, the density of defects and the heat, are predicted [3, 4]. While important aspects of the quantum KZM have been experimentally observed [5–10], the experimental measurement of the heat still remains a significant challenge.

Such non-equilibrium dynamics is of crucial importance ranging from cosmology to condensed matter [11–15]. Yet the existence of scaling laws is not limited to non-equilibrium dynamics across a second-order QPT. It has been predicted that the scaling of some quantities can also occur across a first-order QPT where multiple phases coexist [16–20]. In particular, very recently, the KZM has been generalized to account for a power-law scaling of the temporal onset of spin excitations present in a spinor condensate across the first-order QPT [10]. The generalized KZM (GKZM) has also been experimentally observed in a spinor condensate [10]. Similar to a second-order QPT, it is natural to ask whether the heat can still exhibit a power-law scaling across the first-order QPT.

A spinor Bose-Einstein condensate (BEC), described by a vector order parameter, provides a controllable platform to explore non-equilibrium dynamics, and various interesting relevant phenomena have been experimentally observed [21–28]. In some parameter regime for the condensate, the spin and spatial degrees of freedom are de-

coupled because all spin states have the same spatial wave function under the single-mode approximation [29]. As a consequence, the physics is significantly simplified so that the spin degrees of freedom can be separately studied. For an antiferromagnetic (AFM) sodium condensate, there is a first-order QPT between a polar phase with atoms all occupying the $m_F = 0$ level and an AFM phase with atoms equally occupying the $m_F = \pm 1$ levels, where m_F is the magnetic quantum number. The system thus provides an ideal platform to study the non-equilibrium physics across a first-order QPT.

Here we theoretically and experimentally demonstrate the existence of a power-law scaling of the heat in a sodium spinor condensate for two dynamical processes: a one-way process where a system is driven from a polar phase to an AFM phase and a cyclic process where a system ends up at the initial polar phase. For the one-way process, the power-law scaling is well characterized by the GKZM. In experiments, we prepare an initial condensate in the polar phase and then slowly vary the quadratic Zeeman energy q by controlling magnetic and microwave fields to realize the two non-equilibrium processes. Since the energy gap vanishes at the transition point, adiabaticity cannot be maintained no matter how the system is driven, leading to the appearance of excitations as well as heat, which can be used as a measure of how strongly adiabaticity is broken. Based on Refs. [1, 2], the heat density can be defined as an energy increase per atom relative to the ground state at the final quadratic Zeeman energy q_f over the entire process. In experiments, it can be evaluated by measuring the atom number occupying the $m_F = 0$ level owing to a simple approximate relation between the heat density and the particle number when $|q_f|$ is large.

We start by considering the following Hamiltonian describing a spin-1 BEC under single-mode approximation

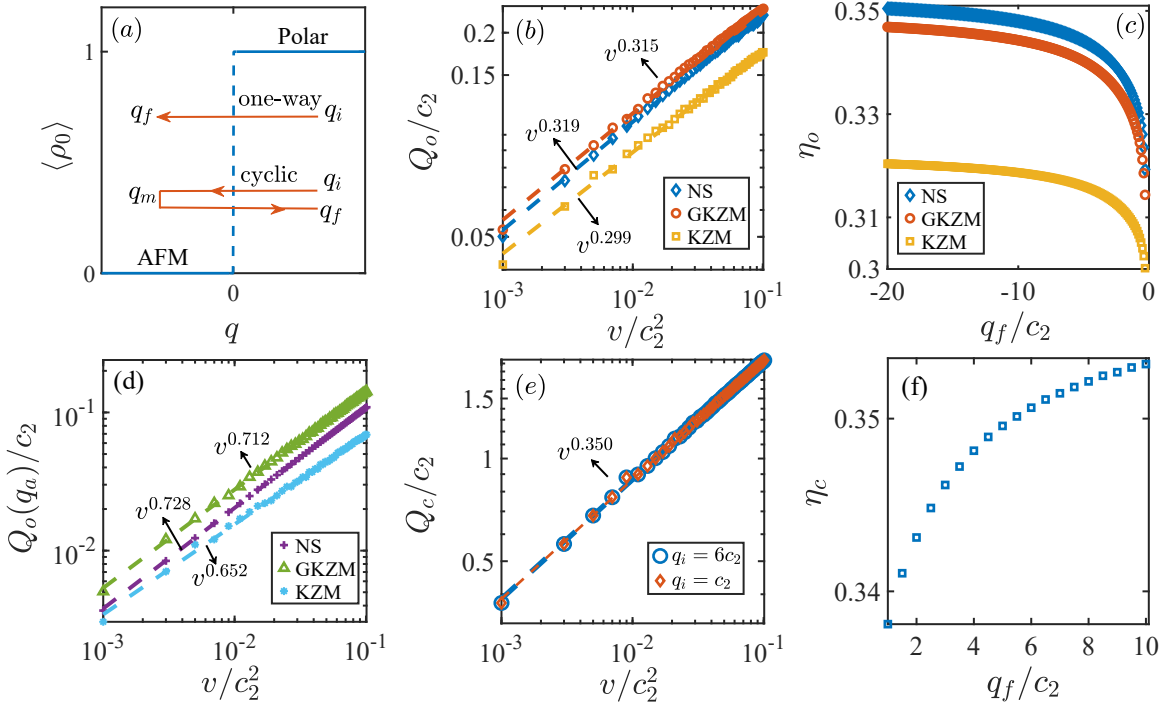


FIG. 1. Schematic illustration of the quench protocol and theoretical demonstration of the heat scaling with respect to the quench rate. (a) The phase diagram depicted by $\langle \rho_0 \rangle$ versus the quadratic Zeeman energy q . Two linear quench protocols are considered: a one-way protocol where q is varied from $q_i > 0$ to $q_f < 0$ and a cyclic protocol where q is changed from $q_i > 0$ to $q_m < 0$ and then back to $q_f > 0$. (b) The scaling of the heat density $Q_o(q_f)$ with the quench rate v for a one-way process with $q_i = c_2$ and $q_f = -0.3c_2$. (c) The scaling exponents η_o of $Q_o(q_f)$ when q_f is set to a range of different values. (d) The scaling of the heat density $Q_o(q_a)$ with the quench rate v for a one-way process with $q_i = c_2$. Here $q_a = -vt_a$ is the corresponding quadratic Zeeman energy at the critical time t_a (see the discussion in the text). In (b-d), the blue diamonds (purple crosses), the red circles (green triangles) and the yellow squares (cyan asterisks) represent the theoretical results for $Q_o(q_f)$ [$Q_o(q_a)$] obtained by the numerical simulation, the GKZM and the KZM, respectively. (e) The scaling of the heat density $Q_c(q_f)$ versus the quench rate v for a cyclic process with $q_f = 6c_2$ and $q_m = -2.5c_2$, where blue circles and red diamonds correspond to $q_i = 6c_2$ and $q_i = c_2$, respectively. (f) The scaling exponents of the heat density for different q_f for a cyclic process with $q_i = c_2$ and $q_m = -2.5c_2$. Here $N = 1.0 \times 10^4$.

$$\hat{H} = c_2 \frac{\hat{\mathbf{L}}^2}{2N} + \sum_{m_F=-1}^1 (qm_F^2 - pm_F) \hat{a}_{m_F}^\dagger \hat{a}_{m_F}, \quad (1)$$

where $\hat{a}_{m_F}^\dagger$ (\hat{a}_{m_F}) is the Boson creation (annihilation) operator for an atom in the hyperfine level $|F = 1, m_F\rangle$, $\hat{\mathbf{L}}$ is the total spin operator with $\hat{L}_\mu = \sum_{i,j} \hat{a}_i^\dagger (f_\mu)_{ij} \hat{a}_j$ ($\mu = x, y, z$) and f_μ being the spin-1 angular momentum matrix, c_2 is the spin-dependent interaction ($c_2 > 0$ for sodium atoms) and N is the total number of atoms. Here p and q describe linear and quadratic Zeeman energies, respectively. In our experiments, we initialize our condensates in the polar phase so that the dynamics is restricted to the eigenspace of $L_z = 0$, since the magnetization along z is conserved, i.e., $[\hat{L}_z, \hat{H}] = 0$. The linear Zeeman term p thus becomes irrelevant in the dynamics even though its value is not equal to zero in the experiment. So the ground states of the spinor condensate correspond to the polar and AFM phases when $q > 0$ and $q < 0$, respectively. The phase diagram is shown in

Fig. 1(a) where the mean value $\langle \rho_0 \rangle$ with $\rho_0 = \hat{a}_0^\dagger \hat{a}_0 / N$ taken as an order parameter drops to zero from one at $q = 0$, indicating the occurrence of the first-order QPT.

We investigate the heat production in two types of quench processes: a one-way process for linearly ramping q from q_i ($q_i > 0$) to q_f ($q_f < 0$) and a cyclic process for linearly ramping q from q_i to q_m ($q_m < 0$) and then back to q_f , forming a cyclic process when $q_f = q_i$ [see Fig. 1(a)]. In both scenarios, we calculate the energy increase at the end of the quench for different ramp rates v . To numerically determine the energy of a spinor condensate, we diagonalize the Hamiltonian under the Fock state basis in the subspace of zero magnetization, $\{|N/2, 0, N/2\rangle, |N/2-1, 2, N/2-1\rangle, \dots, |0, N, 0\rangle\}$, yielding instantaneous eigenstates $|\phi_n(q)\rangle$ ($n = 1, 2, \dots, N/2 + 1$) of $\hat{H}(q)$ satisfying $\hat{H}(q)|\phi_n(q)\rangle = E_n(q)|\phi_n(q)\rangle$. We also solve the Schrödinger equation $i\hbar\partial|\Psi(t)\rangle/\partial t = \hat{H}(t)|\Psi(t)\rangle$ (we take $\hbar = 1$ as a natural unit) to determine the evolving state of the spinor condensate. The energy per atom at the end of the quench is given

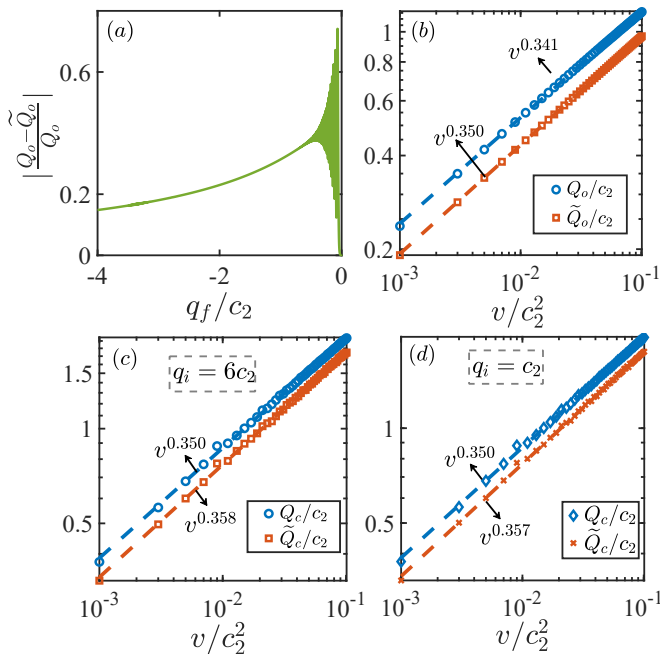


FIG. 2. A comparison between the scaling of the heat density and the quasi-heat density. (a) The relative difference of the quasi-heat density $\tilde{Q}_o(q_f)$ compared to the heat density $Q_o(q_f)$ when $|q_f|$ increases for a fixed quench rate $v = 0.02c_2^2$. A comparison between the scaling of the heat density $Q(q_f)$ and the quasi-heat density $\tilde{Q}(q_f)$ for (b) a one-way process and (c-d) cyclic processes. In (b), $q_i = c_2$ and $q_f = -3c_2$, in (c), $q_i = q_f = 6c_2$ and $q_m = -2.5c_2$, and in (d), $q_i = c_2$, $q_f = 6c_2$ and $q_m = -2.5c_2$. Here $N = 1.0 \times 10^4$.

by $\langle \Psi(q_f) | \hat{H}(q_f) | \Psi(q_f) \rangle = \langle H_I \rangle / N + q_f - q_f \langle \rho_0 \rangle$ with $H_I = c_2 \hat{\mathbf{L}}^2 / (2N)$ characterizing the interactions. Since the corresponding ground state energy per atom in the AFM phase is q_f , the produced heat per atom over the one-way process is given by $Q_o = \langle H_I \rangle / N - q_f \langle \rho_0 \rangle$. For the cyclic process, the produced heat per atom is $Q_c = \langle H_I \rangle / N + q_f (1 - \langle \rho_0 \rangle)$ since the ground state energy of the polar phase is zero.

In Fig. 1(b), we plot our numerical simulation results of the heat density Q_o for a one-way process, remarkably showing the existence of a power-law scaling, i.e., $Q_o \propto v^\eta$ with $\eta = 0.319$. This power-law scaling persists even when q_f is far away from the transition point, but the exponents change as a function of q_f and increase very slowly when $|q_f|$ is large [see Fig. 1(c)]. The exponents are independent of q_i given that two distinct q_i 's are connected by an adiabatic process. For a cyclic process, we also observe the power-law scaling of the heat density Q_c as shown in Fig. 1(e). While the scaling does not depend on q_i for the same reason, Fig. 1(f) shows that the scaling exponents increase slightly with increasing q_f (but they are irrelevant of q_m).

It is a well-known fact that the universal scaling laws across a second-order QPT are accounted for by the

quantum KZM [13–15]. Its essential basis is the existence of impulse and adiabatic regions. Specifically, suppose at $t = 0$, $q = q_c = 0$ and the system is in the polar phase. When we linearly drive the system into the AFM phase, the system cannot respond (impulse region) until the response time $\tau(t_a) = 1/\Delta(t_a) = t_a$, where Δ is the relevant energy gap. When $t > t_a$, adiabaticity is restored (adiabatic region). For a second-order QPT, the relevant energy gap refers to the gap between the ground state and the first excited state. Based on the KZM, the heat induced by a slow quench across the critical point is shown to exhibit a power-law dependence on the ramp rate with the scaling exponent determined by the equilibrium critical exponents [3, 4, 30].

For a first-order QPT, we have demonstrated the existence of impulse and adiabatic regions when a spinor condensate is linearly driven across the transition point [10]. Yet, in stark contrast to the KZM, the relevant energy gap is the gap between the maximally occupied state (the metastable state) and its corresponding first excited state in the first-order case. For example, when $q < 0$, the metastable state refers to the many-body metastable polar phase [10]. We now apply the GKZM to determine the heat scaling. To be more precise, we use the equation $|1/\Delta(t)| = |\Delta(t)/\dot{\Delta}(t)|$ to calculate the critical time t_a and the corresponding $q_a = -vt_a$. Since the evolving state is frozen to the initial state when $t < t_a$, the heat density can be evaluated by $Q_o(q_f) = [\sum_n P_n E_n(q_f) - E_g(q_f)]/N$, where $P_n = |\langle \phi_n(q_a) | \Psi(q_i) \rangle|^2$ is the probability that the initial state $|\Psi(q_i)\rangle$ occupies the eigenstate $|\phi_n(q_a)\rangle$ of $\hat{H}(q_a)$ corresponding to the eigenenergy $E_n(q_a)$.

In Fig. 1(b), we show the power-law scaling of the heat density $Q_o(q_f)$ with respect to v calculated by the GKZM, which agrees very well with the numerical simulation results. Figure 1(c) also displays their comparison of scaling exponents versus q_f , showing very good agreement with less than 1.5% discrepancy. In comparison, we further compute the heat scaling based on the KZM, which exhibits conspicuous discrepancy especially for large $|q_f|$ as shown in Fig. 1(c). For example, when $q_f = -20c_2$, the scaling exponent obtained by the KZM has about 8.6% difference from the numerical simulation results, while the GKZM only exhibits about 1.0% difference. This indicates that the GKZM gives a better account of the heat scaling law at a first-order QPT.

In fact, based on the GKZM, the heat per atom produced during a quench process ending at $q = q_a$ is given by $-q_a$, implying that the heat scaling is determined by the scaling of q_a . In Fig. 1(d), we display the scaling obtained by the numerical simulation, the GKZM and the KZM, demonstrating that the GKZM gives a closer prediction of the power-law exponent to the numerical simulation result than the KZM.

To experimentally probe the heat density is a formidable task due to the complexity of the spin inter-

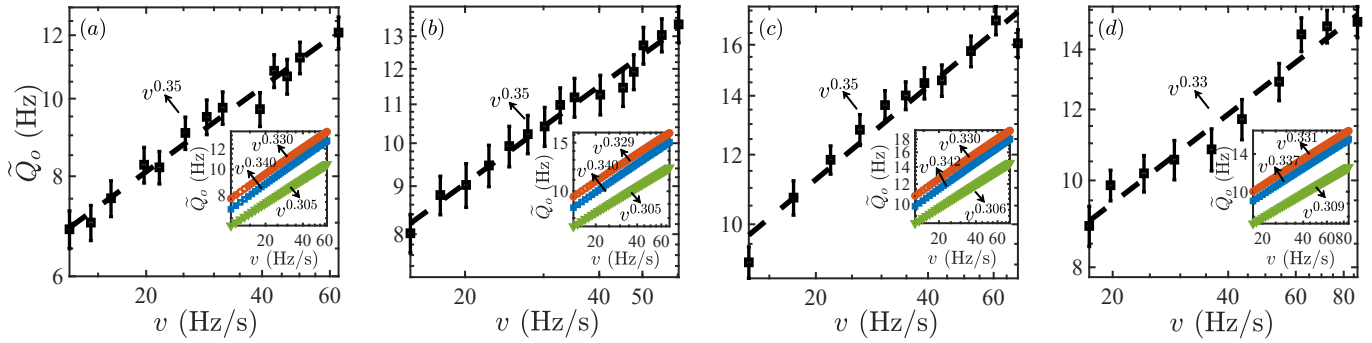


FIG. 3. Experimentally observed power-law scaling of the quasi-heat density \tilde{Q}_o with respect to the ramp rate v for a one-way quench. In (a-c), we consider processes with $q_i \approx 10$ Hz and $q_f = -21.60$ Hz, -24.47 Hz and -28.36 Hz, respectively (see Appendix A for the discussion of the error arising from the calibration of q). For a spinor condensate with about 1100 atoms corresponding to $c_2 = 8.1 \pm 0.9$ Hz (See Appendix B for details on how to experimentally evaluate the value of c_2 and its error). In (d), q is varied from $q_i = 14.33$ Hz to $q_f = -29.11$ Hz for a BEC with about 3000 atoms and $c_2 = 11.8 \pm 0.8$ Hz. The log-log plot of the experimental data are shown as black squares with error bars. The fitting of the data by a power-law function (black dashed line) gives the exponents of 0.35 ± 0.04 in (a), 0.35 ± 0.03 in (b), 0.35 ± 0.06 in (c) and 0.33 ± 0.06 in (d) with 95% confidence interval. Each figure has an inset showing the theoretical results of the scaling of \tilde{Q}_o obtained by the numerical simulation (blue squares), the GKZM (red circles) and the KZM (green triangles). The GKZM with exponents of 0.330, 0.329, 0.330 and 0.331 gives a better account of the power-law scaling with exponents of 0.340, 0.340, 0.342 and 0.337 obtained by the numerical simulation than the corresponding exponents of 0.305, 0.305, 0.306 and 0.309 obtained by the KZM.

actions, which is hard to measure. Fortunately, for the one-way process, when $|q_f|$ is large, the heat density Q_o is dominated by the second part, $\tilde{Q}_o = -q_f \langle \rho_0 \rangle$, which can be experimentally evaluated by measuring $\langle \rho_0 \rangle$ and q_f . We call \tilde{Q}_o the quasi-heat density to distinguish it from the heat density Q_o . Similarly, for the cyclic process, we define the corresponding quasi-heat density as $\tilde{Q}_c = q_f(1 - \langle \rho_0 \rangle)$. For both processes, the heat density and the quasi-heat density are related by the following equation

$$Q_s = \tilde{Q}_s + \langle H_I \rangle / N \quad (2)$$

with $s = o, c$ referring to the one-way and cyclic processes, respectively.

Figure 2(a) shows the decline of the relative difference between the heat density Q_o and the quasi-heat density \tilde{Q}_o when $|q_f|$ is increased; the relative difference decreases to less than 20% when $q_f = -3c_2$ when $v = 0.02c_2^2$. In fact, the scalings determined by these two energy increases agree much better than their energy differences even for not very large $|q_f|$, which is experimentally achievable. For instance, when $q_f = -3c_2$, while there exists 18% difference of \tilde{Q}_o compared to Q_o , their scaling exponents are in excellent agreement with only less than 3% discrepancy for the one-way process [see Fig. 2(b)]. For the cyclic process when $q_f = 6c_2$, the scaling exponent difference is also smaller than 3% [see Fig. 2(c) and (d)]. This allows us to obtain the scaling of the heat density by experimentally measuring $\langle \rho_0 \rangle$ for relatively large $|q_f|$.

In experiments, we produce a sodium BEC in an all-optical trap by evaporation of atoms [27]. At the evapo-

ration cooling stage, we apply a strong magnetic field gradient to remove the atoms on the hyperfine levels $|F = 1, m_F = \pm 1\rangle$ out of the trap, leaving all atoms on the $|F = 1, m_F = 0\rangle$ level. After that, a weak and nearly resonant microwave pulse is applied to excite the atoms from $|F = 1, m_F = 0\rangle$ to $|F = 2, m_F = 0\rangle$ (the corresponding detuning is $\delta \simeq -6$ kHz). Since the atoms on the latter level suffer a significant loss due to three body decay, this process kicks many atoms out of the BEC cloud, resulting in less than 3000 atoms remaining in the trap. The reduction of the atom number allows us to avoid the unwanted relaxation to the AFM ground state when q is tuned to negative values. The atoms are then immersed in a uniform magnetic field with $q_i \approx 10$ Hz for 2 s to equilibrate to the polar phase. Afterwards, we slowly decrease the magnetic field strength so as to linearly vary q according to the relation $q \approx B^2 \cdot 277$ Hz/G². When q is changed to around 5 Hz, we immediately switch on a microwave field with a frequency of 1.7701264 GHz (the detuning is $\delta = -1.5$ MHz relative to the transition from $|F = 1, m_F = 0\rangle$ to $|F = 2, m_F = 0\rangle$) and then gradually raise its amplitude so that q is linearly driven to the negative regime [31] (Appendix A). During the process, the amplitude of the microwave field is precisely controlled by a proportional-integral-derivative (PID) feedback system according to a careful calibration of q 's values. For each quench rate v , ρ_0 is measured by a standard Stern-Gerlach fluorescence imaging at the end of the linear quench in each experiment and $\langle \rho_0 \rangle$ is evaluated by averaging over 40 repeated measurements (Appendix C).

In Fig. 3, we show the experimental results of the quasi-heat density \tilde{Q}_o with respect to the ramp rate v for the

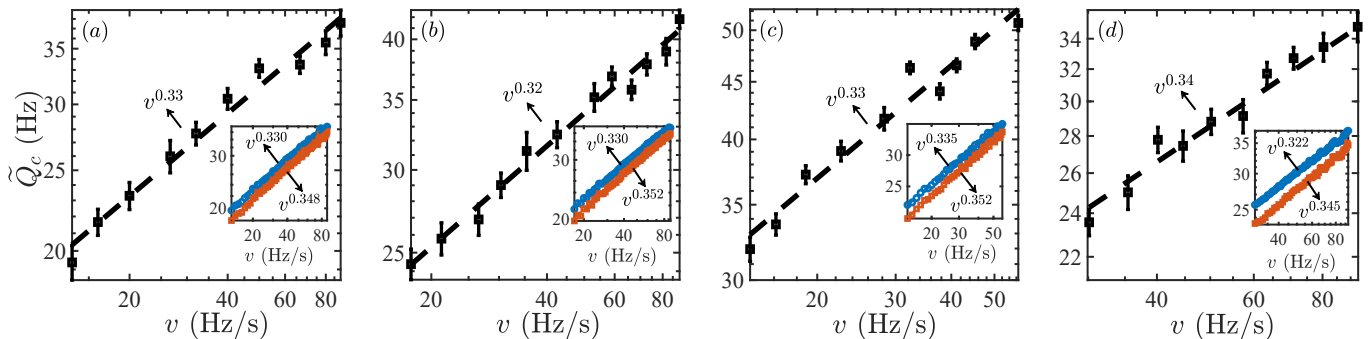


FIG. 4. Experimentally observed power-law scaling of the quasi-heat density \tilde{Q}_c with respect to the quench rate for cyclic processes. In (a-c), q is linearly changed from $q_i \approx 15$ Hz to $q_m = -15.19$ Hz in (a) [$q_m = -22.00$ Hz in (b) and $q_m = -15.49$ Hz in (c)] and then back to the final value $q_f = 60.10$ Hz [$q_f = 66.45$ Hz in (c)] for a condensate with about 1100 atoms corresponding to $c_2 = 8.1 \pm 0.9$ Hz. In (d), the atom number $N = 3000$ corresponding to $c_2 = 11.8 \pm 0.8$ Hz, $q_i = 17.55$ Hz, $q_m = -18.10$ Hz and $q_f = 66.73$ Hz. The experimental data are plotted in the logarithmic scale, which are fitted by power-law functions, giving the exponents of 0.33 ± 0.04 in (a), 0.32 ± 0.03 in (b), 0.33 ± 0.06 in (c) and 0.34 ± 0.05 in (d) under 95% confidence interval. The inset of each figure shows the numerical simulation results of Q_c (blue circles) and \tilde{Q}_c (red squares).

one-way quench with four different sets of quench parameters. In (a-c), we drive a BEC with about 1100 atoms and $c_2 = 8.1 \pm 0.9$ Hz to three distinct q_f . The experimental data clearly demonstrate the existence of a power-law scaling for these different conditions. We fit the data by a power-law function, i.e., $\tilde{Q}_o \propto v^{\tilde{\eta}}$, giving the fitting exponents of $\tilde{\eta} = 0.35 \pm 0.04$, $\tilde{\eta} = 0.35 \pm 0.03$ and $\tilde{\eta} = 0.35 \pm 0.06$, respectively. The results agree well with the numerical simulation results with the power-law fitting exponents of 0.340, 0.340 and 0.342, respectively [see the insets of Fig. 3]. Here the numerically calculated exponents for \tilde{Q}_o exhibit about 10% difference from the exponents of Q_o , which is larger than the result shown in Fig. 2(b) due to larger ramp rates considered here to reduce the relaxation to the ground states in experiments (Appendix D). In Fig. 3(d), we further plot the experimental results for a BEC with roughly 3000 atoms and $c_2 = 11.8 \pm 0.8$ Hz, showing the existence of a power-law scaling with the fitting exponent of 0.33 ± 0.06 , which is in good agreement with the numerically obtained exponent of 0.337.

For a cyclic quench, similar to the one-way one, we initially prepare the condensate in the polar phase with the quadratic Zeeman energy q_i (e.g., $q_i \approx 15$ Hz) provided by a uniform magnetic field and then linearly decrease q to roughly 5 Hz by decreasing the magnetic field strength. After that, we shine a microwave field to the BEC to linearly vary q from about 5 Hz to q_m ($q_m < 0$, e.g., $q_m = -22$ Hz) and then back to 5 Hz by controlling the field amplitude. We then turn off the microwave field and raise the magnetic field strength until q slowly rises to q_f (e.g., $q_f = 60.1$ Hz). Since the results do not depend on the value of q_i when it is sufficiently large so that the dynamics is adiabatic under the quench rate at $q = q_i$ [see Fig. 1(e)], in experiments, we use q_i and q_f with $q_f > q_i$ for experimental convenience. The entire ramping pro-

cess is precisely controlled to be linear according to the calibration of q . Similarly, at the end of each quench, the quasi-heat density \tilde{Q} is measured by probing $\langle \rho_0 \rangle$ through the Stern-Gerlach fluorescence imaging.

For a cyclic quench, in Fig. 4, we show the experimental measurement of the quasi-heat density \tilde{Q}_c as a function of the quench rate v under different quench parameters. For a BEC cloud with about 1100 atoms and $c_2 = 8.1 \pm 0.9$ Hz, the results shown in Fig. 4(a-c) evidently illustrate a power-law scaling of the quasi-heat density with fitting exponents of 0.33 ± 0.04 , 0.32 ± 0.03 and 0.33 ± 0.06 , respectively. The exponents agree well with the exponents of 0.348, 0.352 and 0.352 numerically obtained for \tilde{Q}_c , which are larger than 0.330, 0.330 and 0.335 (numerically calculated scaling exponents for Q_c) by about 5.4%, 6.7% and 5.1%, respectively. This also shows that our experimental measurements cannot differentiate the slight difference between \tilde{Q}_c and Q_c . Additionally, we raise the atom number to around 3000 corresponding to $c_2 = 11.8 \pm 0.8$ Hz and perform the experiments under the quench parameters of $q_i = 17.55$ Hz, $q_m = -18.10$ Hz and $q_f = 66.73$ Hz. Figure 4(d) reveals the existence of a power-law scaling with a fitting exponent of 0.34 ± 0.05 , in good agreement with the numerical result of 0.345.

Our work demonstrates the first experimental observation of a power-law scaling of heat with respect to a ramp rate for non-equilibrium dynamics. Two types of quench processes including one-way and cyclic processes are studied across a first-order QPT in a spinor condensate. The experimentally measured scaling exponents for both non-equilibrium processes agree well with our numerical simulation results.

We thank Yingmei Liu, Ceren Dag, and Anjun Chu for helpful discussions. This work was supported by the Beijing Academy of Quantum Information Sciences,

the National key Research and Development Program of China (2016YFA0301902), Frontier Science Center for Quantum Information of the Ministry of Education of China, and Tsinghua University Initiative Scientific Re-

search Program. Y. Xu also acknowledges the support from the start-up fund from Tsinghua University, the National Natural Science Foundation of China (11974201) and the National Thousand-Young-Talents Program.

APPENDIX A: CALIBRATION OF THE QUADRATIC ZEEMAN ENERGY q

In the experiment, the quadratic Zeeman energy q is contributed by both the magnetic and microwave fields so that

$$q = q_B + q_M, \quad (\text{A1})$$

where q_B and q_M are generated by the magnetic and microwave field, respectively. Specifically, q_B is determined by the magnetic field strength B through $q_B \approx B^2 \cdot 277$ (Hz/G²). Based on the relation $p \approx B \cdot 700$ (KHz/G) with p being the linear Zeeman energy, B can be measured by probing p through a Rabi oscillation between the Zeeman energy level $|F = 1, m_F = 0\rangle$ and $|F = 2, m_F = -1\rangle$. A microwave field at large frequency detuning shifts the energy of the Zeeman levels due to the AC Stark effect and contributes to the quadratic Zeeman energy as

$$q_M = \frac{\Delta E_{m_F=+1} + \Delta E_{m_F=-1} - 2\Delta E_{m_F=0}}{2} \quad (\text{A2})$$

with

$$\Delta E_{m_F} = \frac{1}{4} \sum_{k=-1,0,+1} \frac{\Omega_{m_F, m_F+k}^2}{\Delta_{m_F, m_F+k}}, \quad (\text{A3})$$

where Ω_{m_F, m_F+k} is the Rabi frequency for the resonant transition from $|F = 1, m_F\rangle$ to $|F = 2, m_F+k\rangle$ and Δ_{m_F, m_F+k} is the microwave detuning relative to the transition between these energy levels.

In the experiment, the magnetic field strength is controlled by a voltage V_B that determines the magnitude of the current flowing through the Helmholtz coils. In Fig. A1(a), we show the measured q_B as a function of the voltage V_B , which is well fitted by a parabola function, thus allowing us to linearly change q_B by controlling V_B .

To determine the microwave quadratic Zeeman energy q_M , we experimentally evaluate the Rabi frequencies $\Omega_{0,-1}$, $\Omega_{0,1}$ and $\Omega_{-1,-1}$ by probing the Rabi oscillations for a resonant transition between the two corresponding energy levels. Other Rabi frequencies can be calculated according to the following relations

$$\Omega_{0,1} = \sqrt{3}\Omega_{-1,0}, \quad \Omega_{1,2} = \sqrt{6}\Omega_{-1,0}, \quad (\text{A4})$$

$$\Omega_{1,1} = \Omega_{-1,-1} = \frac{\sqrt{3}}{2}\Omega_{0,0}, \quad (\text{A5})$$

$$\Omega_{0,-1} = \sqrt{3}\Omega_{1,0}, \quad \Omega_{-1,-2} = \sqrt{6}\Omega_{1,0}. \quad (\text{A6})$$

We now fix the microwave's frequency at 1.7701264 GHz with a detuning $\Delta_{0,0} = -1500$ kHz for the transition from $|F = 1, m_F = 0\rangle$ to $|F = 2, m_F = 0\rangle$. q_M is then calculated based on Eq. (A2). Since the magnetic field still exists with $q_B \approx 5.0$ Hz when the microwave pulse is applied, the total quadratic Zeeman energy $q = q_M + q_B$. Because the Rabi frequencies depend on the microwave field amplitude, we can control the amplitude to vary q_M and q . In our experiment, we stabilize the amplitude of the microwave pulse by a PID system and calibrate the values of q at several different microwave amplitudes controlled by the feedback voltage V_f . The measured q with respect to V_f is displayed in Fig. A1(b) with a parabola fitting to the data allowing for a linear ramp of q by tuning V_f .

To estimate the error between the calibrated q and the true value of q , we apply a sudden quench method to measure the transition point $q_c = 0$. Specifically, we initialize the condensate in the polar phase with $q_i > 0$ and then suddenly change q to q_f . After 500 ms' evolution, we probe the atom populations on the $m_F = 0$ state. If $q_f > 0$, then all atoms should remain on the $m_F = 0$ state; otherwise, if $q_f < 0$, atoms will show up on the $m_F = \pm 1$ level. In the experiment, the sudden quench of q is realized by switching on the microwave field with the frequency of 1.7701264 GHz and a certain amplitude controlled by V_f . Since q_f decreases as V_f increases [see Fig. A1(b)], we can find a maximum V_f^{\max} so that all the atoms stay on the $m_F = 0$ state and a minimum V_f^{\min} so that atoms begin to show up on the $m_F = \pm 1$ states. The calibrated value of the transition point q_c is thus $q_{\text{cali}} = [q(V_f^{\min}) + q(V_f^{\max})]/2$, resulting in a calibration error of $\delta q = q_{\text{cali}} - q_c = q_{\text{cali}}$ for each set of data. We summarize the calibration error δq for 21 days' measurements in Table A1.

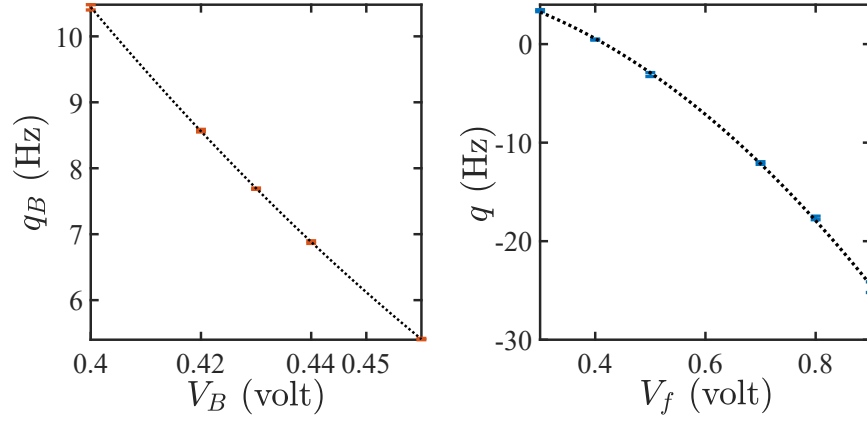


FIG. A1. (Color online) Experimental calibration of the quadratic Zeeman energy q . (a) Experimentally measured q_B (black crosses) as a function of the voltage V_B . (b) Experimentally measured q (black crosses) as a function of the feedback voltage V_f of the PID system. The experimental data are fitted by the red dashed parabola curves.

$q(V_f^{max})(\text{Hz})$	$q(V_f^{min})(\text{Hz})$	$q_{cali}(\text{Hz})$	$\delta q(\text{Hz})$
-1.03	-1.11	-1.07	
0.43	0.35	0.39	
0.15	0.07	0.11	
-0.62	-0.85	-0.74	
-0.83	-1.06	-0.95	
0.35	0.28	0.32	
-1.16	-1.37	-1.27	
0.13	0.06	0.10	
-0.12	-0.17	-0.15	
0.20	0.13	0.17	
-1.43	-1.63	-1.53	-0.45 ± 0.70
-1.23	-1.44	-1.34	
0.40	0.33	0.37	
0.29	0.22	0.26	
-1.04	-1.25	-1.15	
0.31	0.20	0.26	
-1.13	-1.34	-1.24	
0.32	0.25	0.29	
0.01	-0.27	-0.13	
-1.32	-1.53	-1.43	
-0.64	-0.84	-0.74	

TABLE A1. Summary of the measured values of $q(V_f^{max})$ and $q(V_f^{min})$ obtained through sudden quench experiments performed during 21 days. The calibrated value of q in each row is obtained by $q_{cali} = (q(V_f^{max}) + q(V_f^{min}))/2$, giving the calibration error $\delta q = \bar{q}_{cali} + \sigma$ where \bar{q}_{cali} is the mean value of q_{cali} and σ is the standard deviation.

APPENDIX B: MEASUREMENT OF c_2

The spin-dependent interaction coefficient c_2 can be measured by observing the spin oscillation, i.e., time evolution of ρ_0 when the condensate is initially prepared to the state $|\rho_1, \rho_0, \rho_{-1}\rangle$ with $\rho_1 = \rho_{-1}$ and $0 < \rho_0 < 1$. According to the mean-field theory, where the quantum fluctuations are neglected and the operators are replaced by their expectation values, the spin-mixing dynamical equations for the spin-1 condensate are given by [32]

$$\dot{\rho}_0 = \frac{2c_2}{\hbar} \rho_0 \sqrt{(1 - \rho_0)^2 - m^2} \sin\theta, \quad (\text{B1})$$

$$\dot{\theta} = -\frac{2q}{\hbar} + \frac{2c_2}{\hbar} (1 - 2\rho_0) + \left(\frac{2c_2}{\hbar}\right) \frac{(1 - \rho_0)(1 - 2\rho_0) - m^2}{\sqrt{(1 - \rho_0)^2 - m^2}} \cos\theta, \quad (\text{B2})$$

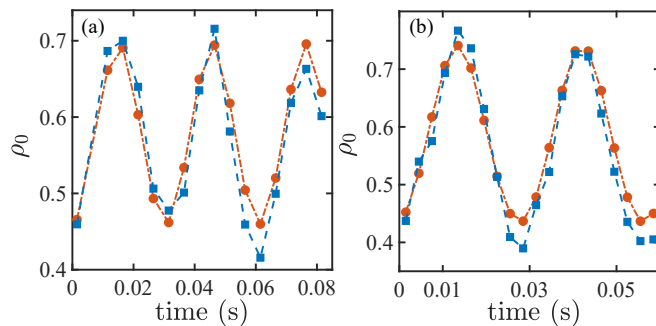


FIG. B1. (Color online) Spin oscillation measurements of c_2 by fitting the experimentally observed time evolution of ρ_0 (blue squares) by theoretical simulations (red circles). In (a) [(b)], the initial state is prepared to $|0.28, 0.46, 0.26\rangle$ ($|0.30, 0.44, 0.26\rangle$) for a system with about 1100 (3000) atoms and $q = 14.31$ Hz ($q = 14.22$ Hz).

$q(\text{Hz})$	$\theta(\times\pi)$	$c_2(\text{Hz})$	$\bar{c}_2(\text{Hz})$	N
14.31	0.99	8.0	$8.1 \pm 0.9\text{Hz}$	1100
17.15	0.97	7.4		
24.09	1.01	9.8		
27.69	1.01	8.2		
31.91	1.15	7.3		
9.44	0.95	12.6	$11.8 \pm 0.8\text{Hz}$	3000
11.62	0.91	11.4		
14.22	0.95	11.4		
17.17	0.97	10.8		
20.45	1.05	12.9		

TABLE B1. Summary of the datasets for c_2 's measurements.

where $m = \rho_1 - \rho_{-1}$ is the magnetization and $\theta = \theta_+ + \theta_- - 2\theta_0$ is the relative phase. By fixing the quadratic Zeeman energy q and $m \approx 0$, we simulate the time evolution of ρ_0 to find the value of c_2 that best fits the experimental results. c_2 is then obtained by averaging over 5 measurements for 5 distinct q . In Fig. B1(a) and (b), we show the experimental and theoretical results of the time evolution of ρ_0 with the initial state being $|\rho_1, \rho_0, \rho_{-1}\rangle = |0.28, 0.46, 0.26\rangle$ for $N = 1100$ and $|\rho_1, \rho_0, \rho_{-1}\rangle = |0.30, 0.44, 0.26\rangle$ for $N = 3000$, respectively. In Table B1, we summarize the five measured results for different atom numbers, giving the mean value of c_2 of 8.1 ± 0.9 Hz for $N = 1100$ and 11.8 Hz ± 0.8 Hz for $N = 3000$.

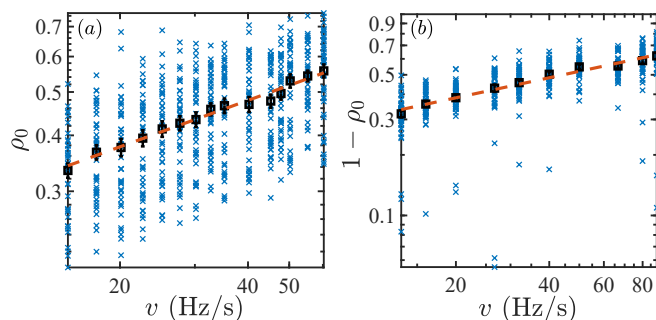


FIG. B2. (Color online) Log-log plots of the measured ρ_0 (blue diagonal crosses) and their mean values (black squares). (a) A one-way quench process with $N \approx 1100$, $q_i = 9.96$ Hz and $q_f = -24.47$ Hz. (b) A cyclic quench process with $N \approx 1100$, $q_i = 15.04$ Hz, $q_m = -15.19$ Hz and $q_f = 60.1$ Hz. The red dashed lines denote the linear fits of $\langle \rho_0 \rangle$.

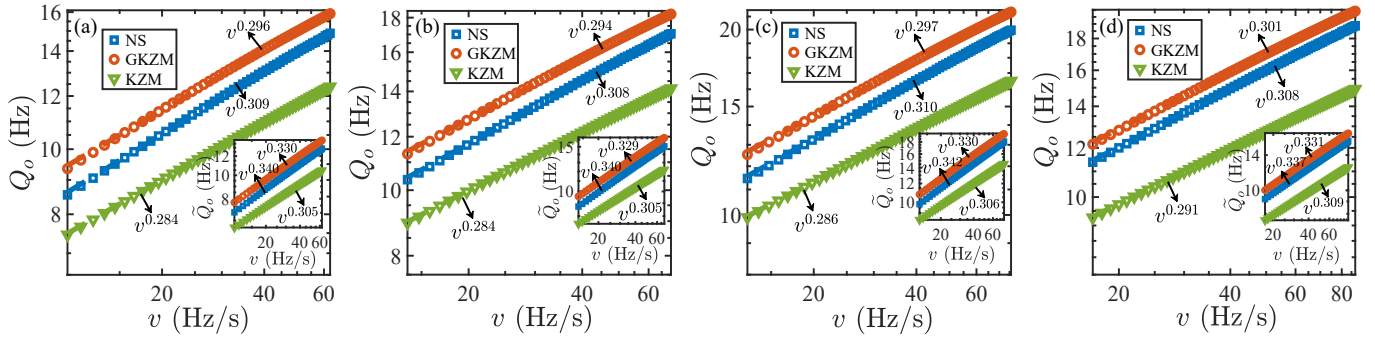


FIG. D1. (Color online) Comparison of the theoretical results of Q_o and \tilde{Q}_o corresponding to Fig. 3 in the main text. The quench parameters are the same as in Fig. 3. The results by numerical simulation, the KZM and the GKZM are plotted as blue squares, green triangles and red circles, respectively. The inset shows the theoretical results of \tilde{Q}_o as a comparison to those of Q_o .

$v(c_2^2)$	η	$\tilde{\eta}$	$ \eta - \tilde{\eta} /\eta$
0.001 ~ 0.01	0.370	0.373	0.81%
0.011 ~ 0.1	0.351	0.356	1.42%
0.1 ~ 1	0.315	0.343	8.89%

TABLE D1. Finite quench rate effects on the scaling exponents for Q_o and \tilde{Q}_o in the one-way quench process with $q_i = c_2$, $q_f = -3c_2$ and $N = 1100$. Different ranges of ramp rates v give different scaling exponents η , $\tilde{\eta}$ and their relative difference.

APPENDIX C: EXPERIMENTAL MEASUREMENT OF ρ_0

In experiments, we measure ρ_0 by the standard Stern-Gerlach fluorescence imaging for different ramp rates. Fig. B2(a) shows the measured data (labelled by blue diagonal crosses) of ρ_0 for a one-way process where q is linearly varied from 9.96 Hz to -24.47 Hz. In this case, the atom number N is restricted to about 1100 corresponding to a fluorescence count in the range of 2.5×10^9 and 2.8×10^9 . $\langle \rho_0 \rangle$ at each ramp rate is calculated by averaging over measurements repeated 40 times, which is plotted as black squares in the figure. The error bars of $\langle \rho_0 \rangle$ (the error in the mean) originate from the quantum fluctuations and the measurement fluctuations and is evaluated as $\sigma/\sqrt{40}$ [33], where σ is the standard deviation of the 40 samples. For the one-way quench process, $\tilde{Q}_o = -q_f \langle \rho_0 \rangle$ and thus the error bar of \tilde{Q}_o can be evaluated by

$$\delta\tilde{Q}_o = \sqrt{(\langle \rho_0 \rangle^{\text{var}} + \langle \rho_0 \rangle^2)(q_f^{\text{var}} + q_f^2) - (\langle \rho_0 \rangle q_f)^2}, \quad (\text{C1})$$

where the superscript var denotes the variance of a quantity. Since there is an error of -0.45 Hz for q_f , we make a correction of $+0.45$ Hz to q_f with the variance $q_f^{\text{var}} = 0.70^2 (\text{Hz})^2 = 0.49 (\text{Hz})^2$ according to the calibration of q in Table. A1. In Fig. B2(b), we also display the original data of $\langle \rho_0 \rangle$ for a cyclic process, where q is changed from 15.04 Hz to -15.19 Hz and then back to 60.1 Hz at different ramp rates for a system with roughly 1100 atoms.

APPENDIX D: FINITE QUENCH RATE EFFECTS ON SCALING EXPONENTS

In Fig. D1, we provide the numerical simulation results of Q_o , showing about 10% difference for \tilde{Q}_o compared with Q_o . This discrepancy is larger than the result shown in Fig. 2(b) in the main text. We attribute this discrepancy to the finite ramp rates. As shown in Table D1, the relative difference is larger for a range of quench rates with larger values due to larger contribution of interactions to total energy for a fixed q_f . In our experiments, both q_f and quench rate v that can be taken are limited by the applied microwave field which can induce the relaxation of the condensate to the AFM ground state when its amplitude is strong or it is applied for a long time. To reduce the relaxation effect, we take the minimum q_f as -29.11 Hz and the slowest ramp rate as 10 Hz/s corresponding to about 3 s for an quench process during which the microwave field is shined to vary the quadratic Zeeman energy.

† yongxuphy@tsinghua.edu.cn

* These authors contributed equally to this work.

‡ lmduan@tsinghua.edu.cn

- [1] Polkovnikov, A. Microscopic Expression for Heat in the Adiabatic Basis. *Phys. Rev. Lett.* **101**, 220402 (2008).
- [2] Polkovnikov, A. & Gritsev, V. Breakdown of the adiabatic limit in low-dimensional gapless systems. *Nat. Phys.* **4**, 477-481 (2008).
- [3] Polkovnikov, A., Sengupta, K., Silva, A. & Vengalattore, M. Colloquium: Nonequilibrium dynamics of closed interacting quantum systems. *Rev. Mod. Phys.* **83**, 863 (2011).
- [4] De Grandi, C. & Polkovnikov, A. Adiabatic Perturbation Theory: From Landau-Zener Problem to Quenching Through a Quantum Critical Point. In *Quantum Quenching, Annealing and Computation* pp. 75-114 (Springer, Berlin, Heidelberg, 2010).
- [5] Chen, D., White, M., Borries, C. & DeMarco, B. Quantum Quench of an Atomic Mott Insulator. *Phys. Rev. Lett.* **106**, 235304 (2011).
- [6] Anquez, M. et al. Quantum Kibble-Zurek Mechanism in a Spin-1 Bose-Einstein Condensate. *Phys. Rev. Lett.* **116**, 155301 (2016).
- [7] Clark, L. W., Feng, L. & Chin, C. Universal space-time scaling symmetry in the dynamics of bosons across a quantum phase transition. *Science* **354**, 606-610 (2016).
- [8] Zhang, J., Cucchiatti, F. M., Laflamme, R. & Suter, D. Defect production in non-equilibrium phase transitions: experimental investigation of the Kibble-Zurek mechanism in a two-qubit quantum simulator. *New J. Phys.* **19**, 043001 (2017).
- [9] Keesling, A. et al. Quantum Kibble-Zurek mechanism and critical dynamics on a programmable Rydberg simulator. *Nature* **568**, 207-211 (2019).
- [10] Qiu, L.-Y. et al. Observation of generalized Kibble-Zurek mechanism across a first-order quantum phase transition in a spinor condensate. *Sci. Adv.* **6**, eaba7292 (2020).
- [11] Kibble, T. W. Some implications of a cosmological phase transition. *Phys. Rep.* **67**, 183-199 (1980).
- [12] Zurek, W. H. Cosmological experiments in superfluid helium? *Nature* **317**, 505-508 (1985).
- [13] Damski, B. The Simplest Quantum Model Supporting the Kibble-Zurek Mechanism of Topological Defect Production: Landau-Zener Transitions from a New Perspective. *Phys. Rev. Lett.* **95**, 035701 (2005).
- [14] Zurek, W. H., Dorner, U. & Zoller, P. Dynamics of a quantum phase transition. *Phys. Rev. Lett.* **95**, 105701 (2005).
- [15] Polkovnikov, A. Universal adiabatic dynamics in the vicinity of a quantum critical point. *Phys. Rev. B* **72**, 161201 (2005).
- [16] Panagopoulos, H. & Vicari, E. Off-equilibrium scaling behaviors across first-order transitions. *Phys. Rev. E* **92**, 062107 (2015).
- [17] Liang, N. & Zhong, F. Renormalization-group theory for cooling first-order phase transitions in Potts models. *Phys. Rev. E* **95**, 032124 (2017).
- [18] Coulamy, I. B., Saguia, A. & Sarandy, M. S. Dynamics of the quantum search and quench-induced first-order phase transitions. *Phys. Rev. E* **95**, 022127 (2017).
- [19] Pelissetto, A. & Vicari, E. Dynamic off-equilibrium transition in systems slowly driven across thermal first-order phase transitions. *Phys. Rev. Lett.* **118**, 030602 (2017).
- [20] Shimizu, K., Hirano, T., Park, J., Kuno, Y. & Ichinose, I. Dynamics of first-order quantum phase transitions in extended Bose-Hubbard model: from density wave to superfluid and vice versa. *New J. Phys.* **20**, 083006 (2018).
- [21] Sadler, L. E., Higbie, J. M., Leslie, S. R., Vengalattore, M. & Stamper-Kurn, D. M. Spontaneous symmetry breaking in a quenched ferromagnetic spinor Bose-Einstein condensate. *Nature* **443**, 312-315 (2006).
- [22] Leslie, L. S., Hansen, A., Wright, K. C., Deutsch, B. M. & Bigelow, N. P. Creation and Detection of Skyrmions in a Bose-Einstein Condensate. *Phys. Rev. Lett.* **103**, 250401 (2009).
- [23] Choi, J., Kwon, W. J. & Shin, Y. Observation of Topologically Stable 2D Skyrmions in an Antiferromagnetic Spinor Bose-Einstein Condensate. *Phys. Rev. Lett.* **108**, 035301 (2012).
- [24] Kronjäger, J., Becker, C., Soltan-Panahi, P., Bongs, K. & Sengstock, K. Spontaneous Pattern Formation in an Antiferromagnetic Quantum Gas. *Phys. Rev. Lett.* **105**, 090402 (2010).
- [25] Guzman, J. et al. Long-time-scale dynamics of spin textures in a degenerate $F = 1$ ^{87}Rb spinor Bose gas. *Phys. Rev. A* **84**, 063625 (2011).
- [26] Parker, C. V., Ha, L.-C. & Chin, C. Direct observation of effective ferromagnetic domains of cold atoms in a shaken optical lattice. *Nat. Phys.* **9**, 769-774 (2013).
- [27] Yang, H.-X. et al. Observation of dynamical quantum phase transitions in a spinor condensate. *Phys. Rev. A* **100**, 013622 (2019).
- [28] Tian, T. et al. Observation of dynamical quantum phase transitions with correspondence in an excited state phase diagram. *Phys. Rev. Lett.* **124**, 043001 (2020).
- [29] Kawaguchi, Y. & Ueda, M. Spinor Bose-Einstein condensates. *Phys. Rep.* **520**, 253-381 (2012).
- [30] Xue, M., Yin, S. & You, L. Universal driven critical dynamics across a quantum phase transition in ferromagnetic spinor atomic Bose-Einstein condensates. *Phys. Rev. A* **98**, 013619 (2018).
- [31] Luo, X.-Y. et al., Deterministic entanglement generation from driving through quantum phase transitions. *Science* **355**, 620 (2017).
- [32] Zhang, W., Zhou, D. L., Chang, M.-S., Chapman, M. S., and You, L., Coherent spin mixing dynamics in a spin-1 atomic condensate, *Phys. Rev. A* **72**, 013602 (2005).
- [33] Ross, S. M., Introductory Statistics, Academic Press, Fourth Edition (2017).